Kinetic theory of FENE dumbell in confined flow under applied pressure and electric fields

Petr Hotmar*, Ravi Chella†

Department of Chemical and Biomedical Engineering,
Florida State University

Abstract

We extend the kinetic theory of dilute polymer solutions under external pressure and electric fields [10] to a) include finite chain extensibility and b) properly account for wall-induced hydrodynamic interactions due to charged polymers in an electrolyte. Focusing on cross-stream migration due to individual and combined effects of these fields, we conclude that the thickness of the depletion layer is overpredicted by the Hookean spring model and scales quadratically with the Peclet number, similar to the dependence on Weissenberg number reported in shear flows. We show the variation of molecular stretch and normal stresses across the channel and derive migration tensors for the Green's function of Stokes flow in a Debye-Hückel electrolyte.

Keywords: *kinetic theory, cross-stream migration, Poiseuille flow, electric field, polyelectrolyte*

1 Introduction

Constitutive theories of dilute polymer solutions fail to capture some important phenomena arising in non-homogeneous flows with spatially nonuniform velocity gradients and stresses. Polymer migration, for instance, can instead be treated with sufficient accuracy in terms of the phase-space kinetic theory, which describes a molecular model of the polymer in terms of a configurational distribution function [1]. The theory has recently been extended to include a wall correction in the hydrodynamic interaction tensor due to a

---

*email: ph06@fsu.edu

†email: rchella@fsu.edu

point force acting near a planar wall [13] and subsequently, using a Hookean spring model in pressure-driven flow, to account for the wall-induced hydrodynamic interactions arising from a unidirectional external force [9]. Such force typically represents gravity (in sedimentation studies) or electric field (in DNA electrophoresis). The use of an infinitely extensible spring, however, is a severe approximation which can yield incorrect rheological properties [2], especially in flows with significant stretching. Furthermore, it has been shown [17] that in confinement, the spring laws are different due to the broken symmetry of the underlying random walk representation, with the net effect being a reduced extensibility of the chain. This motivates an extension of the above study to a FENE model with adjustable stiffness. Another deficiency of the existing theory for polyelectrolytes is the absence of wall corrections for point charges immersed in an electrolyte and surrounded by counter-ion clouds, which precludes correct prediction of cross-stream migration patterns, especially when the Debye length is finite. We thus develop a model which addresses the above deficiencies and apply it to electrophoresis where hydrodynamic interactions (HIs) are assumed to be only partially screened, in agreement with recent experimental findings [9].

The layout of this paper is as follows. After reviewing the basic kinetic theory equations in Sec. 2.1 and 2.2, we show conditions under which an external force can be treated within the standard kinetic theory model in Sec. 2.3. Also in Sec. 2.3, we derive an orientational distribution function (ODF) for a potential flow of FENE dumbells with wall-induced migration due to a general external force. Then in Sec. 3.1 we specialize to a Poiseuille flow (characterized by a Weissenberg number Wi) and unidirectional force (characterized by a Peclet number Pe), showing an explicit form for the ODF as well as the differential equation governing the center-of-mass distribution function (CDF). Sec. 3.2 discusses the limitations and applicability of the employed theory, which is then applied in Sec. 3.3-3.5 to examine cross-stream migration due to separate and combined effects of imposed flow and external force. In Sec. 3.6-3.7 we discuss the dependence of the depletion layer, normal stress differences and molecular stretch on Wi and Pe. In Sec. 4.1 we discuss the image system for the electrophoretic Stokeslet (ES), which represents a point-force disturbance due to charged beads in an electrolyte under Stokes flow. First we show the conditions under which the image system for the standard Stokeslet (which decays with distance as $1/r$) can be used in place of the ES (which decays as $1/r^3$). Then we restrict ourselves to the long-range part of the ES and derive the corresponding migration tensors based on the image system for a potential dipole, which produces an equivalent disturbance field. Sec. 4.2 presents migration results

2

for the ES, analogous to those in Sec. 3.3-3.5.

2   Background

Dumbell models are simplified representations of polymer molecules. While the limited number of internal degrees of freedom restricts their use to low-frequency flows, they have been shown to provide valid predictions of rheological properties in non-Newtonian fluids [2] and allow for tractable analysis of polymer migration in confined geometries.

A dilute polymer solution is thus modeled by a suspension of non-interacting dumbells immersed in a continuous Newtonian solvent of viscosity η. The two spring-connected beads of a flexible dumbell follow equations of motion, which combine with a continuity equation to yield the Fokker-Planck equation of the kinetic theory.

2.1   Equations of motion and continuity in the kinetic theory

Denoting the bead position vectors of the dumbell as $\boldsymbol{r}_1$ and $\boldsymbol{r}_2$, we can write continuity equations for the positional and orientational distribution functions $n(\mathbf{r_c})$ and $\psi(\mathbf{r_c}, \mathbf{Q})$, respectively, as

$$\frac{\partial}{\partial \boldsymbol{r}_c} \cdot (\langle \dot{\mathbf{r}}_c \rangle n) = 0,$$
$$\frac{\partial}{\partial \mathbf{Q}} \cdot (\dot{\mathbf{Q}} \psi) = 0, \tag{1}$$

where the center-of-mass $\boldsymbol{r}_c = (\boldsymbol{r}_1 + \boldsymbol{r}_2)/2$ and the bond vector $\mathbf{Q} = (q_1, q_2, q_3) = \boldsymbol{r}_2 - \boldsymbol{r}_1$ provide a convenient coordinate system and $\langle \cdot \rangle$ denotes an ensemble average with respect to ψ, i.e. $\langle \cdot \rangle = \int \cdot \psi d\mathbf{Q}$.

The force balance between the Brownian $\boldsymbol{F}^b$, spring $\boldsymbol{F}^s$, electric $\boldsymbol{F}^e$ and hydrodynamic forces $\boldsymbol{F}^h$ yields the velocity of the i-th bead, which can be rewritten in terms of the center-of-mass $\dot{\boldsymbol{r}}_c$ and bond vector $\dot{\mathbf{Q}}$ velocities, with the imposed velocity field Taylor-expanded around $\mathbf{r_c}$ to quadratic order in $\mathbf{Q}$. The experiments [6] and simulations [13] confirmed the existence of near-wall depletion layers of thickness much larger than the polymer size, justifying the neglect of a steric wall force from the force balance. After substituting $\boldsymbol{F}^b = -k_b T \frac{\partial \ln \Psi}{\partial \mathbf{r}}$, where $\Psi(\mathbf{r_c}, \mathbf{Q}) = n(\mathbf{r_c}) \psi(\mathbf{r_c}, \mathbf{Q})$, k_b is the

Boltzmann constant and T is temperature, one obtains [5]

$$\dot{\mathbf{r}}_c = \boldsymbol{u} + \frac{1}{8}\mathbf{QQ} : \nabla\nabla\boldsymbol{u} + \frac{1}{2}\bar{\boldsymbol{\Omega}} \cdot \boldsymbol{F}^s + \frac{2}{k_bT}\boldsymbol{D_K} \cdot \boldsymbol{F}^e + \frac{k_bT}{2}\bar{\boldsymbol{\Omega}} \cdot \frac{\partial \ln \Psi}{\partial \mathbf{Q}} - \boldsymbol{D_K} \cdot \frac{\partial \ln \Psi}{\partial \mathbf{r_c}},$$

$$\dot{\mathbf{Q}} = \mathbf{Q} \cdot \nabla\boldsymbol{u} - \left(2\mu\boldsymbol{I} + \hat{\boldsymbol{\Omega}}\right) \cdot \boldsymbol{F}^s - \bar{\bar{\boldsymbol{\Omega}}} \cdot \boldsymbol{F}^e - k_bT\left(2\mu\boldsymbol{I} + \hat{\boldsymbol{\Omega}}\right) \cdot \frac{\partial \ln \Psi}{\partial \mathbf{Q}} + \frac{k_bT}{2}\bar{\bar{\boldsymbol{\Omega}}} \cdot \frac{\partial \ln \Psi}{\partial \mathbf{r_c}},$$

$$\tag{2}$$

where $\boldsymbol{D_K}, \hat{\boldsymbol{\Omega}}, \bar{\boldsymbol{\Omega}}$ and $\bar{\bar{\boldsymbol{\Omega}}}$ are linear functions of the HI tensor

$$\boldsymbol{\Omega}_{ij} \equiv (1 - \delta_{ij})\boldsymbol{S}_{ij} + \boldsymbol{G}_{ij}, \tag{3}$$

with the Oseen-Burgers Stokeslet $\boldsymbol{S}$, wall correction $\boldsymbol{G}$ and Stokes friction coefficient $\mu^{-1} = \zeta$. The above functions of the HI tensor are discussed further in our previous work [8]. To simplify subsequent computations, the wall correction tensor $\boldsymbol{G}$, which is based on the superposition of two fundamental solutions to Stokes equation due to Blake [3] near two planar boundaries, is linearized around $\mathbf{r_c}$ to arrive at $\hat{\boldsymbol{\Omega}}, \bar{\boldsymbol{\Omega}}$ and $\bar{\bar{\boldsymbol{\Omega}}}$ which are linear in $\mathbf{Q}$. The equations of motion (Eq. 2) then serve as a starting point for further analysis of cross-stream migration phenomena in a slit.

2.2 Fokker-Planck equation for the orientational distribution function

For simplicity and following [9], the only HI tensor retained in the continuity equation (Eq. 1) is the $\bar{\bar{\boldsymbol{\Omega}}} \cdot \mathbf{F}^e$ term, which is essential to capture the migration due to external force. The terms in the expression for the bond vector velocity in Eq. 2 that contain $\hat{\boldsymbol{\Omega}}$ and $\bar{\bar{\boldsymbol{\Omega}}}$ are neglected. Using Eq. 2, we thus obtain

$$0 = \frac{\partial}{\partial \mathbf{Q}} \cdot \left[(\boldsymbol{\kappa} \cdot \mathbf{Q})\psi - 2k_bT\mu\frac{\partial}{\partial \mathbf{Q}}\psi - 2\mu\mathbf{F}^s\psi - \bar{\bar{\boldsymbol{\Omega}}} \cdot \mathbf{F}^e\psi \right], \tag{4}$$

where $\boldsymbol{\kappa} \equiv (\nabla\boldsymbol{u})^T$ is the gradient of the imposed velocity field.

Our goal is to solve Eq. 4 first for a general homogeneous flow $\boldsymbol{u} = \boldsymbol{\kappa} \cdot \mathbf{Q}$ and a nonlinear FENE spring force, where $\mathbf{F}^s = a(Q)\mathbf{Q}$, with

$$a(Q) = \frac{H}{1 - \left(\frac{Q}{Q_0}\right)^2}, \quad Q = |\mathbf{Q}|, \tag{5}$$

Hookean spring constant H and maximum spring extension Q_0.

Eq. 4 is a stationary Fokker-Planck equation, $0 = \mathrm{L_{FP}}\psi$, where the Fokker-Planck operator is

$$\mathrm{L_{FP}} = -\frac{\partial}{\partial \mathbf{Q}} \cdot \boldsymbol{D}(\mathbf{Q}) + \frac{\partial}{\partial \mathbf{Q}} \cdot \frac{\partial}{\partial \mathbf{Q}} \boldsymbol{\Delta}(\mathbf{Q}), \tag{6}$$

with possibly nonlinear drift vector

$$\boldsymbol{D}(\mathbf{Q}) = \boldsymbol{\kappa} \cdot \mathbf{Q} - \frac{2}{\zeta} a(Q)\mathbf{Q} - \bar{\bar{\boldsymbol{\Omega}}} \cdot \mathbf{F}^e, \tag{7}$$

and constant diffusion tensor

$$\boldsymbol{\Delta}(\mathbf{Q}) = \frac{2k_b T}{\zeta} \boldsymbol{I}, \tag{8}$$

where we denote $\frac{\partial}{\partial \mathbf{Q}} \cdot \boldsymbol{D}(\mathbf{Q}) = \sum_i \frac{\partial}{\partial q_i} D_i(\mathbf{Q})$.

With linear drift and constant diffusion, the distribution function ψ will be Gaussian [9]. An analytical solution can be found even for nonlinear drift, provided that the condition detailed balance is satisfied [15]. Expressed in terms of potential conditions,

$$\frac{\partial D_i}{\partial q_j} = \frac{\partial D_j}{\partial q_i}, \tag{9}$$

the solution, up to an integration constant, is then

$$\psi = e^{-\phi(\mathbf{Q})}, \tag{10}$$

where the potential function

$$\phi(\mathbf{Q}) = -\frac{\zeta}{2k_b T} \int^{\mathbf{Q}} D_i(\mathbf{Q}')dq_i' \tag{11}$$

and the Einstein summation convention is invoked.

2.3   External force

Assuming uni-directional electric force $\boldsymbol{F}^e = F^e \boldsymbol{e}_1$ and given the linearization discussed in Sec. 2.1, we have the components $[\omega_{ij}]_{1 \leq i,j \leq 3}$ of $\bar{\bar{\boldsymbol{\Omega}}}$ all linear

in $\mathbf{Q}$, i.e. we can write $\omega_{ij} = \sum_{k=1}^{3} \alpha_k^{i,j} q_k$. Then

$$\left[\bar{\bar{\boldsymbol{\Omega}}} \cdot \mathbf{F}^e\right]_i = \left[\sum_{j=1}^{3} \left(\sum_{k=1}^{3} \alpha_k^{i,j} q_k\right) F_j\right]_i$$

$$= \left[\sum_{k=1}^{3} \left(\sum_{j=1}^{3} \alpha_k^{i,j} F_j\right) q_k\right]_i$$

$$= \left[\sum_{k=1}^{3} \mu_{ik} q_k\right]_i = [\boldsymbol{\mu} \cdot \mathbf{Q}]_i, \quad \text{for i=1,2,3.} \quad (12)$$

Thus, when the action of $\bar{\bar{\boldsymbol{\Omega}}}$ on the external force yields a linear transformation in $\mathbf{Q}$, we have $\bar{\bar{\boldsymbol{\Omega}}} \cdot \mathbf{F}^e = \boldsymbol{\mu} \cdot \mathbf{Q}$, and the first and last terms in Eq. 7 can be combined to give

$$\hat{\boldsymbol{\kappa}} \cdot \mathbf{Q}, \quad \text{where } \hat{\boldsymbol{\kappa}} \equiv \boldsymbol{\kappa} - \boldsymbol{\mu}. \quad (13)$$

This part of the drift then describes the influence of the non-equilibrium phenomena (flow and external forces), while the remaining term, associated with $\boldsymbol{F}^s$, can be explicitly evaluated by use of Eqs. 10 and 11 to give the equilibrium distribution function ψ_{eq}. We thus obtain the standard form of ψ valid for a steady-state potential flow [2], $\psi = \psi_{eq}\phi_{fl}$, however with $\boldsymbol{\kappa}$ in ϕ_{fl} replaced by $\hat{\boldsymbol{\kappa}}$; note that $\phi_{fl} \propto e^{\hat{\boldsymbol{\kappa}}:\mathbf{QQ}}$ is a dimensionless factor which contains information about the flow pattern.

With the linearized $\bar{\bar{\boldsymbol{\Omega}}}$ of the form,

$$\bar{\bar{\boldsymbol{\Omega}}} = \lambda(y) \begin{bmatrix} -q_y & q_x & 0 \\ -q_x & -2q_y & -q_z \\ 0 & q_z & -q_y \end{bmatrix}, \quad (14)$$

we obtain a traceless, symmetric dyad

$$\boldsymbol{\mu} = \lambda(y) \begin{bmatrix} F_y & -F_x & 0 \\ -F_x & -2F_y & -F_z \\ 0 & -F_z & F_y \end{bmatrix}. \quad (15)$$

Using the chain rule and the identities $\frac{\partial}{\partial \mathbf{Q}} a(Q) = \frac{\mathbf{Q}}{Q} \frac{d}{dQ} a(Q)$ and $\frac{\partial}{\partial \mathbf{Q}} \cdot (\boldsymbol{\tau} \cdot \mathbf{Q}) = \text{Tr}(\boldsymbol{\tau})$, we can now rewrite the Fokker-Planck equation (Eq. 4) as

$$\frac{2k_b T}{\zeta} \frac{\partial}{\partial \mathbf{Q}} \cdot \frac{\partial}{\partial \mathbf{Q}} \psi - \left(\hat{\boldsymbol{\kappa}} : \frac{\partial \psi}{\partial \mathbf{Q}} \mathbf{Q}\right) + \frac{2a}{\zeta} \mathbf{Q} \cdot \frac{\partial \psi}{\partial \mathbf{Q}} + \frac{2}{\zeta} \left[Q \frac{da}{dQ} + 3a\right] \psi = 0. \quad (16)$$

6

For $\hat{\boldsymbol{\kappa}} = \hat{\boldsymbol{\kappa}}^T$ and the FENE spring force, the potential conditions are satisfied and ψ can be obtained directly from Eqs. 10 and 11. Thus for potential flow of FENE dumbells with wall-induced HIs, we have

$$\psi = \psi_{eq}\phi_{fl} = \frac{1}{J}\left(1 - \left(\frac{Q}{Q_0}\right)^2\right)^b e^{\zeta M}, \tag{17}$$

where J is the normalization constant, b is the stiffness ratio of time constants describing FENE (λ_Q) and Hookean (λ_H) dumbells,

$$\lambda_Q = \frac{\zeta Q_0^2}{12k_bT}, \quad \lambda_H = \frac{\zeta}{4H}, \quad b \equiv 3\frac{\lambda_Q}{\lambda_H} = \frac{HQ_0^2}{2k_bT}, \tag{18}$$

and

$$M = q_x^2(\kappa_{11} - \lambda F_y) + q_y^2(\kappa_{22} + \lambda 2F_y) - q_z^2(\kappa_{11} + \kappa_{22} + \lambda F_y)$$
$$+ 2q_xq_y(\kappa_{12} + \lambda F_x) + 2q_xq_z\kappa_{13} + 2q_yq_z(\kappa_{23} + \lambda F_z). \tag{19}$$

3 Stokeslet in neutral solution

3.1 FENE model with wall-induced HIs and external force

To relax the potential flow requirement we expand the distribution function, given in Eq. 17, in a perturbation series in the powers of the velocity gradients. Retaining the first two corrections, we obtain the same form as Bird [2], however with the rate-of-strain $\dot{\boldsymbol{\gamma}}$ and vorticity $\boldsymbol{\omega}$ tensors now expressed in terms of $\hat{\boldsymbol{\kappa}}$, yielding the final form

$$\psi = \psi_{eq}(1 + \phi_1 + \phi_2 + \dots) = \frac{1}{J_{eq}}\left[1 - \frac{Q}{Q_0}^2\right]^{b/2}\left(1 + Z(\dot{\boldsymbol{\gamma}} : \mathbf{QQ})\right.$$

$$\left. + Z^2\left[-\frac{Q_0^4}{b_{5,1}b_{7,1}}(\dot{\boldsymbol{\gamma}} : \dot{\boldsymbol{\gamma}}) + \frac{4Q_0^2}{b_{7,2}}\left(1 - \frac{1}{2}\left(\frac{Q}{Q_0}\right)^2\right)(\{\dot{\boldsymbol{\gamma}} \cdot \boldsymbol{\omega}\} : \mathbf{QQ}) + \frac{1}{2}(\dot{\boldsymbol{\gamma}} : \mathbf{QQ})^2\right] + \dots\right), \tag{20}$$

where $b_{[i,j]} \equiv i + jb$, $J_{eq} = \frac{\pi^{3/2}Q_0^3\Gamma(b_{1,1})}{\Gamma(b_{\frac{5}{2},1})}$, Γ is the gamma function and $Z = \frac{\zeta}{8k_bT}$.

Note that $\boldsymbol{\kappa}$ is not required to be position-independent, allowing for non-homogeneous flows. Assuming plane Poiseiulle flow with an effective, position-dependent shear rate $\dot{\gamma}(y) = 2\bar{\dot{\gamma}}\left(1 - 2\frac{y}{h}\right)$, where $\bar{\dot{\gamma}}$ is the mean shear

rate, y is the orthogonal distance of the center-of-mass from the channel wall and h is the channel height, we obtain the non-dimensionalized distribution function

$$\psi = G(1 - Q^2)^b \left(b_{5,2}b_{7,2} + 2(P_1 + 2P_2) \left(b_{5,2}b_{7,2}q_x q_y + \left(-1 + b_{5,2}(-2 + Q^2)q_y^2\right.\right.\right.$$
$$+\ b_{5,2}q_x^2 \left(2 - Q^2 + b_{7,2}q_y^2\right)\right) P_1 + \left(-2 + 2b_{5,2}b_{7,2}q_x^2 q_y^2\right) P_2\right)\right),$$

$$(21)$$

where $G(b) = \frac{Q_0^3}{J_{eq}b_{5,2}b_{7,2}}$, $P_1 = 3Wi_Q \left(1 - 2\frac{y}{h}\right)$ and $P_2 = \frac{9}{256}Pe \left(\frac{1}{y^2} - \frac{1}{(y-h)^2}\right)$. The Weissenberg number Wi_Q is defined in terms of the FENE time constant λ_Q as $Wi_Q = \lambda_Q \bar{\gamma}$ and the Peclet number Pe is based on the magnitude of the external force F^e, $Pe = \frac{F^e a}{\zeta D_0}$, where a is the bead radius and $D_0 = \frac{k_b T}{2\zeta}$.

While the natural length scale here is Q_0, we would like to allow for the comparison with the results for a Hookean spring [9]. Therefore, throughout the rest of the work all the lengths ($\mathbf{Q}, y, h, a$) are scaled by $R_g = \sqrt{\frac{3k_b T}{4H}}$, the equilibrium radius of gyration for the Rouse chain [2]. This necessitates the inclusion of the rescale factor $R = Q_0/R_g = \sqrt{\frac{8}{3}b}$ in the equations below. Note that with the length scale R_g, $Wi_Q = \frac{R^2}{4}Wi_H$, where $Wi_H = \lambda_H \bar{\gamma}$ is defined in terms of the Hookean time constant λ_H.

To further facilitate comparison with the previous theoretical study [9], we note that the fluid Peclet number Pe_f^K and the Peclet number Pe^K used in [9] reduce, respectively, to $Pe_f^K = 6Wi$ and $Pe^K = Pe/a$, where hereafter we set $Wi = Wi_H$. The values of Wi and Pe used in the plots of the center-of-mass distribution correspond, respectively, to the values of Pe_f^K and Pe^K used in the study. Similarly, we set the channel height and bead radius to the same values as used in the numerical simulations of multi-bead chains [9, 16], i.e. $h = 8$ and $a = \frac{1}{8}$ (which corresponds to the hydrodynamic interaction parameter [11] $h^* = a/\sqrt{\pi} \approx 0.07$). We scale the center-of-mass concentration $n(y)$ by its average, $n_t = \int_0^h n(y')dy'$, effectively normalizing it, i.e. $\int_0^h \frac{n(y')}{n_t}dy' = 1$. The FENE model results were obtained with the ratio $b = 1$, which characterizes a stiff polymer chain with limited flexibility.

In a steady state, the flux of the center-of-mass probability distribution function $n(\mathbf{r}_c)$ normal to the wall must vanish; using Eq. 2, we obtain

$$n\langle \dot{\mathbf{r}}_c \rangle \cdot \mathbf{e}_y = 0 = f(b, y, h, a, Wi, Pe)$$
$$= \frac{9}{8}ba\lambda \langle A(q_x^2 - 2q_y^2 + q_z^2) \rangle + \frac{3}{4}Pe\langle \hat{S}_{yx} \rangle$$
$$- \frac{3}{4}a\frac{\partial}{\partial y}\langle \hat{S}_{yy} \rangle - \left(1 + \frac{3}{4}a\langle \hat{S}_{yy} \rangle - \frac{9}{4}a\omega\right)\frac{\partial}{\partial y}\ln n, \qquad (22)$$

8

where $A = A(Q) = \frac{1}{R^2 - Q^2}$, $\lambda = \lambda(y, h) = \frac{1}{y^2} - \frac{1}{(y-h)^2}$, $\omega = \omega(y, h) = \frac{1}{y} - \frac{1}{y-h}$, and the non-dimensionalized Stokeslet $\hat{\boldsymbol{S}}(\mathbf{Q}) = 6\pi\eta R_g \boldsymbol{S} = \frac{1}{Q}\left(\boldsymbol{I} + \frac{\mathbf{QQ}}{Q^2}\right)$.

The first term in Eq. 22 can be written more generally as $\langle \bar{\bar{\boldsymbol{\Omega}}} \cdot \mathbf{F}^s \rangle$ (as in [9]) or as a double dot product of a third order constant migration tensor $\boldsymbol{M}$ and a polymeric contribution to the stress tensor $\boldsymbol{\tau^p}$, yielding $\boldsymbol{M} : \boldsymbol{\tau^p}$ (as in [13]).

3.2 Applicability of the perturbation series solution

Since the perturbation series expansion of the distribution function is around the equilibrium distribution, the convergence rate deteriorates as the Weissenberg and Peclet numbers increase, while slows flows show good convergence [2]. For strong flows (large Wi and/or Pe), stiff springs ($b \to 0$), small bond vector ($Q \to 0$) and/or polymer center-of-mass close to the walls ($y \to 0, h$), the function becomes negative in the corresponding defective region. This increases error in the ensemble averages of quantities that are non-negligible in the defective region, namely components of $\boldsymbol{S}$. One consequence is a proportionate deviation of the diffusivity (see below) from unity.

While a finite depletion layer thickness (discussed in Sec. 3.6) effectively excludes the polymer from the near-wall regions for large enough Wi and Pe, the ranges of Wi and Pe have to be restricted to ensure convergence. The near-wall regions are thus excluded from integrals over the channel height. We further confirmed that the negativeness of the distribution functions depends only weakly on both Pe and Wi.

3.3 Migration due to flow

For convenience, in the pressure-driven flow (plane Poiseiulle flow) we set the transverse diffusivity (coefficient of the last term in Eq. 22) to unity. This approximation, which prevents the diffusivity from becoming negative near the walls due to the use of approximate HI tensors (Sec. 3.2), has been shown to lead to a small qualitative difference in the concentration profiles near the centerline [9]. Neglecting the diffusivity gradient $\frac{\partial}{\partial y}\langle S_{yy}\rangle$ for the moment and setting the external force to zero (Pe=0), we solve Eq. 22 by separation of variables to, yielding

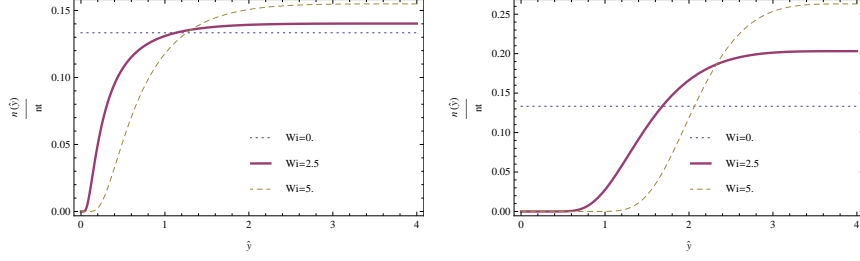$$n(y) = \hat{n}(W) = C \exp\left[-\frac{81Na}{8}\left(\frac{h}{W} + \frac{4}{h}\ln(W)\right)Wi^2\right],$$

Fig. 1: Center-of-mass distribution for different Wi. No external force, diffusivity gradient neglected. Left: FENE spring model, right: Hookean spring model.
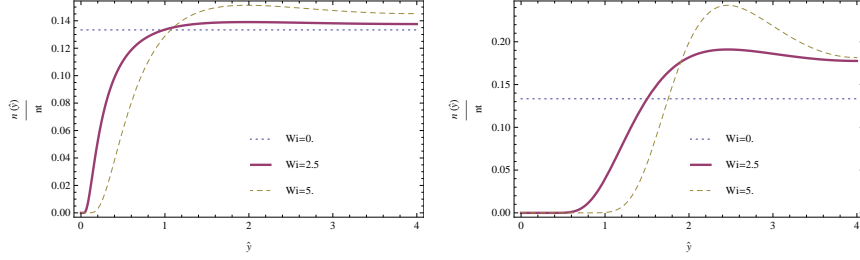

Fig. 2: Center-of-mass distribution for different Wi. No external force, diffusivity gradient included. Left: FENE spring model, right: Hookean spring model.

where $N(b) = \frac{\Gamma(b_{\frac{5}{2}},1)b_{7,5}}{\Gamma(b_{\frac{9}{2}},1)b_{7,2}}$ and $W = y(h - y)$ (a scaled velocity profile of the Poiseiulle flow). Scaling n by n_t eliminates the constant of integration C.

In Fig. 1, we see the characteristic depletion layer at the wall and a uniform distribution near the centerline. When the diffusivity gradient is included, we observe the typical dip along the centerline (confirmed both experimentally and in simulations [13]), reflecting polymer migration towards the wall, Fig. 2. This phenomenon is addressed further in our Brownian dynamics simulations [8]. The corresponding plots for the Hookean spring model in Figs. 1 and 2, suggest that a linear spring model severely over-predicts the thickness of both the depletion layer and the transition layer between the depletion layer and the bulk region. Additionally, the concentration in the bulk region is in fact much closer to the uniform concentration (corresponding to the equilibrium $Wi = 0$) than the Hookean spring model indicates.
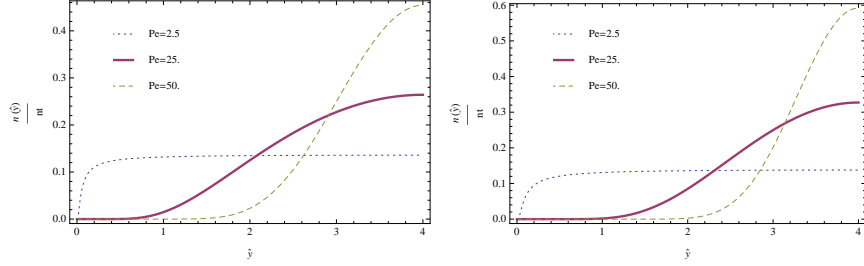
10

Fig. 3: Center-of-mass distribution for different Pe. No imposed flow. Left: FENE spring model, right: Hookean spring model.

3.4 Migration due to external force

To explore the effects due to the external force only, we set $Wi = 0$. For simplicity, and in agreement with the assumption of near-wall region exclusion, we neglect terms proportional to W^{-n}, where $n \geq 3$. Equation 22 then gives

$$\hat{n}(W) = \exp\left[-\frac{75Mh}{4W}Pe^2\right],$$

where $M(b) = \frac{\Gamma(b_{\frac{5}{2},1})}{\Gamma(b_{3,1})R\sqrt{\pi}}$.

In Fig. 3 we see the development of the depletion layer with the thickness proportional to Pe, for both FENE and Hookean spring models, respectively. The depletion layer is again over-predicted by the linear spring model.

3.5 Migration due to flow and external force

With both the pressure flow and external force included, the migration towards the centerline will be either enhanced (flow and force in cooperation, $Pe < 0$, Fig. 4) or reduced (flow and force in competition, $Pe > 0$, Fig. 5). Neglecting the diffusivity gradient and the terms proportional to W^{-n} where $n \geq 3$, Eq. 22, rewritten in terms of W, reduces to

$$\frac{\partial \ln \hat{n}(W)}{\partial W} = \frac{3M}{5h}WiPe + \frac{75Mh}{4W^2}Pe^2 + \frac{81Na(h^2 - 4W)}{8hW^2}Wi^2. \tag{23}$$

The solution is then

$$\hat{n}(W) = \exp\left[\frac{3MW}{5h}WiPe - \frac{75Mh}{4W}Pe^2 - \frac{81Na}{8}\left(\frac{h}{W} + \frac{4}{h}\ln(W)\right)Wi^2\right]. \tag{24}$$
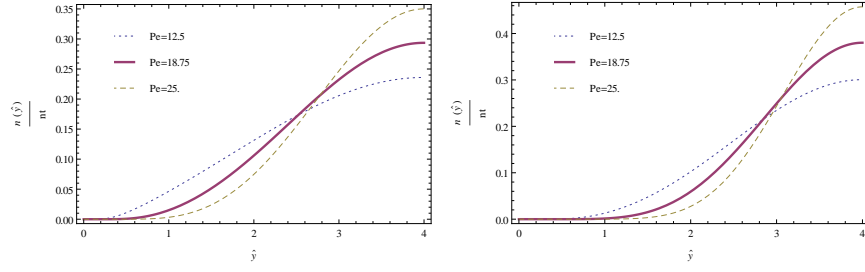
Fig. 4: Center-of-mass distribution. Flow and force in cooperation, $Wi = 5/6$. Left: FENE spring model, right: Hookean spring model.
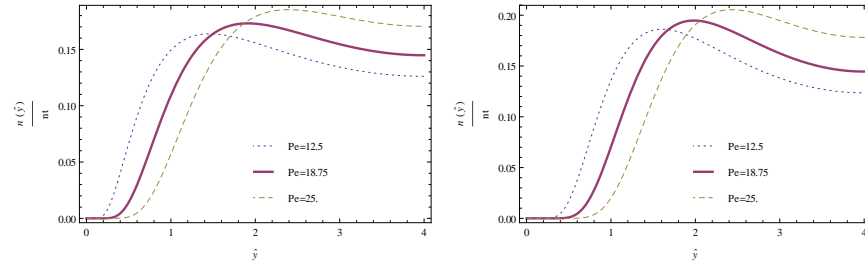

Fig. 5: Center-of-mass distribution. Flow and force in opposition, $Wi = 5/6$. Left: FENE spring model, right: Hookean spring model.

The use of approximate hydrodynamic interaction tensors in the development of the equations above gives rise to unrealistically large values of n near the walls (i.e. when $W \to 0$). These regions are thus excluded from the corresponding integrals (see Sec. 3.2 for more details on the applicability of the perturbation series expansion). The error has been shown negligible [9], primarily because the polymer is subject to steric wall repulsion in the near-wall region, as discussed in Sec. 2.1.

The center-of-mass distribution functions for the FENE spring should, however, be interpreted qualitatively. For the stiff spring used in this work ($b = 1$), the neglect of $\hat{\boldsymbol{\Omega}}$ in Eq. 2 may lead to non-negligible error as the large spring force will yield a qualitatively different orientation distribution function ψ.

3.6 Depletion layer scaling

The scaling behavior of the depletion layer thickness near a planar wall has been studied in a steady shear flow ($v_x = \dot{\gamma} y$, where $\dot{\gamma}$ is the shear rate). A power law scaling $L_d \propto Wi^\alpha$ has been observed in Brownian dynamics simulations [13, 7], with $\alpha = 2$ and $2/3$ in the limit of small and large Wi, respectively. To examine the transition between the two scaling regimes, we use an approximate constitutive equation for FENE dumbells, which has the form [2]

$$Z\boldsymbol{\tau}_p + \lambda_H \boldsymbol{\tau}_{p(1)} - \lambda_H[\boldsymbol{\tau}_p - \epsilon nk_bT\boldsymbol{I}]\frac{D\ln Z}{Dt} = -\epsilon nk_bT\lambda_H\dot{\boldsymbol{\gamma}}_{(1)}, \qquad (25)$$

where $\boldsymbol{\tau}_p$ is the polymer contribution to the stress tensor (with the total stress tensor $\boldsymbol{\tau} = -\eta_s\dot{\gamma} + \boldsymbol{\tau}_p$, where η_s is the solvent viscosity), $\dot{\boldsymbol{\gamma}} = \nabla\boldsymbol{v} + [\nabla\boldsymbol{v}]^T$ is the rate-of-strain tensor, $\epsilon = \frac{b}{2+b}$ and $Z = 1 + \frac{3}{b}\left(\epsilon - \frac{\text{Tr}(\boldsymbol{\tau}_p)}{3nk_bT}\right)$. The material derivative and first convected derivative of a second-order tensor $\boldsymbol{\tau}$ are denoted, respectively, as $\frac{D}{Dt}\boldsymbol{\tau} = \frac{\partial}{\partial t}\boldsymbol{\tau} + \boldsymbol{v}\cdot\nabla\boldsymbol{\tau}$ and $\boldsymbol{\tau}_{(1)} = \frac{D}{Dt}\boldsymbol{\tau} - [(\nabla\boldsymbol{v})^T\cdot\boldsymbol{\tau} + \boldsymbol{\tau}\cdot(\nabla\boldsymbol{v})]$. Solving Eq. 25 for the individual components of the polymer stress tensor in steady shear and substituting the first and second normal stress differences $N_1 = \tau_{xx} - \tau_{yy}$ and $N_2 = \tau_{yy} - \tau_{zz}$ into Ma's expression for the depletion layer thickness near a planar wall [13], $L_d = \frac{9}{16}a\frac{N_1-N_2}{nk_bT}$, we obtain

$$L_d = \frac{3b(5+b)\sinh\left[\frac{1}{3}\text{arcsinh}\left[\frac{3\sqrt{\frac{3}{2}}(2+b)\text{Wi}}{(5+b)^{3/2}}\right]\right]^2}{4(2+b)}a. \qquad (26)$$

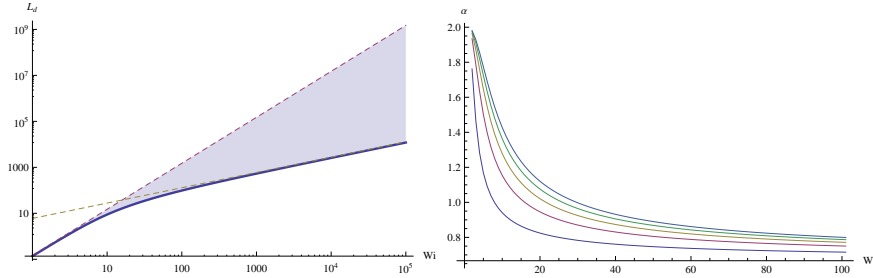**Fig. 6:** Left: $L_d \propto Wi^{\alpha_{1,2}}$. The deviation from the quadratic scaling ($\alpha_1 = 2$) is shaded. As $Wi \to \infty, \alpha_2 \to 2/3$. b=500 (nearly Hookean spring), the dashed lines correspond to the $\alpha_{1,2}$ scalings. Right: The transition between the power-law regimes $L_d \propto Wi^\alpha$ for $b = 1$ (bottom), $100, 200, 300, 400$ and 500 (top).

For the hydrodynamic interaction parameter $h^* = 0.07$, Fig. 6 shows deviation of L_d from the quadratic scaling with increasing Wi, with the transition between the two scaling regimes occurring at $Wi \approx 20$. The transition is steep for small values of b and becomes more gradual with the increasing spring flexibility.

To examine the behavior of the depletion layer in plane Poiseuille flow, we can define, in a manner similar to [13], the steady-state depletion layer thickness L_d as the dominant length scale of the exponential in Eq. 24. Recognizing that W^{-1} goes to infinity faster than linear or logarithmic functions of W, we set

$$L_d^W = \frac{75Mh}{4}Pe^2 + \frac{81Nah}{8}Wi^2 \qquad \left(W \ll \frac{h}{2}\right). \qquad (27)$$

We thus obtain quadratic scalings $L_d^W \sim Wi^2$ and $L_d^W \sim Pe^2$; the former scaling has been observed [13] in low Weissenberg number shear flow in the vicinity of a single wall.

To provide an independent measure of L_d, we compute it as the value of y where the center-of-mass distribution $n_c(y)$ is equal to $\alpha = 0.1\%$ of its maximum value at the center of the channel, i.e. $n/n_c = \alpha$. The dependence of L_d on Wi, Pe and the stiffness ratio b is depicted in Fig. 7-8, with L_d scaled by half the channel width. As expected, Fig. 7 confirms that in a slit, L_d saturates along the centerline for large Wi and Pe, i.e. $\lim_{Wi,Pe \to \infty} L_d = H/2$. For fixed Pe we observe decrease in the power-law exponent with increasing Wi. This decrease becomes gradually less pronounced as Pe increases, with the depletion layer thickness becoming independent of Wi for large Pe. Similar comments apply to the dependence on Wi for fixed Pe.
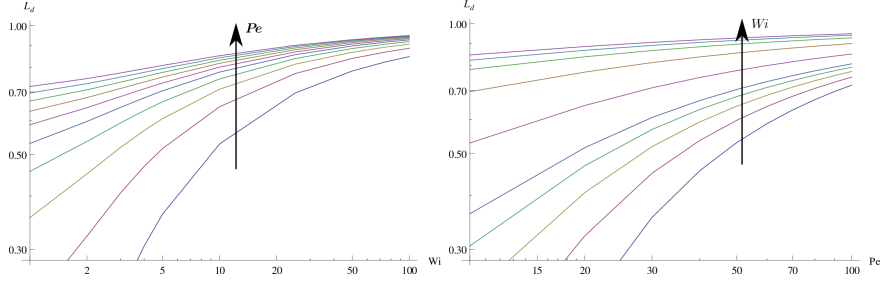
Fig. 7: Left: L_d dependence on Wi, for $Pe = 10, 20 \ldots 100$ with $b = 10$ (stiff dumbell). Right: L_d dependence on Pe for $Wi = 1, 2 \ldots 100$ with $b = 10$. Solid lines intended as a guide to the eye.
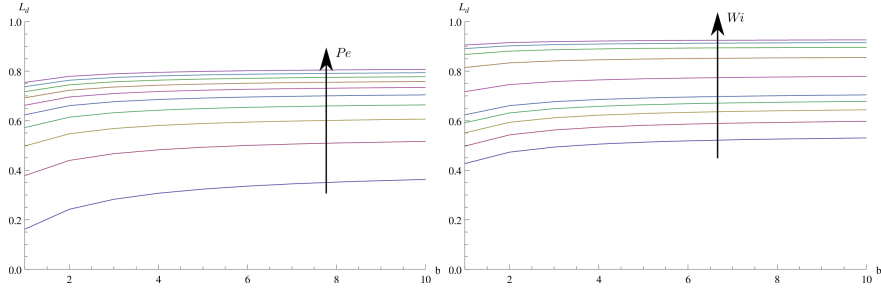

Fig. 8: Left: L_d dependence on b for $Pe = 10, 20 \ldots 100$ with $Wi = 5$. Right: L_d dependence on b for $Wi = 1, 2 \ldots 100$ with $Pe = 50$. Solid lines intended as a guide to the eye.

Fig. 8 suggests that for large strength of flow or external force, as quantified by Wi and Pe, the difference between using a FENE spring or Hookean spring diminishes, seeing that L_d is approaching its maximum value for the given (Wi, Pe) pair.

To explore in greater detail the behavior near $Wi \approx 0$, we approximated $W \log[W]$ appearing in the equation for L_d by its Taylor series expansion around $W = 1$ up to the second order and solved the resulting algebraic equation to arrive at an analytical expression valid for small Wi, which yields an almost constant dependence on Wi, with a mild increase near $Wi = 1$. Combined with the curves valid for large Wi (Fig. 7 left), we note a sigmoidal dependence of L_d on Wi with saturation at about 90% for large Wi.
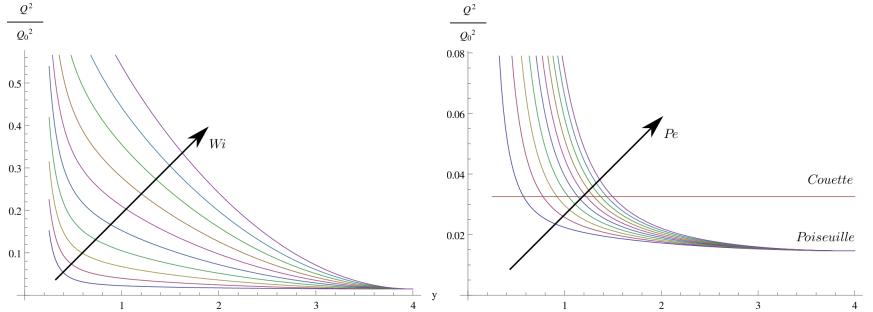
15

Fig. 9: Left: Stretch for $b = 100$ and $Pe = 1$. The curves correspond to $Wi = 0.5, 1, 1.5, \ldots 5$. Right: Stretch for $b = 100$ and $Wi = 1$. The curves correspond to $Pe = 1, 2, 3 \ldots 10$.. The horizontal line corresponds to the theoretical value in steady shear flow.

3.7 Molecular stretch and normal stress differences

The ratio of $\langle Q^2 \rangle$ to its equilibrium value $Q_0 = \langle Q^2 \rangle_{eq}$ can serve as an indicator of molecular stretching in a given flow. Fig. 9 depicts molecular stretch across the channel width for different Wi and Pe. We observe the stretch is monotonically decreasing to its minimum value at the center of the channel, where the shear stress is zero. Comparing the stretch at the centerline of our pressure-driven flow to the theoretical stretch for FENE dumbells in steady-state shear flow [2] (where $\frac{\langle Q^2 \rangle}{Q_0^2} = \frac{3}{b+5}[1 + \frac{2b^2(b+2)}{3(b+5)(b+7)(b+9)}Wi^2]$), we find the former to be at 45% of the latter.

The stress tensor calculation may also help validate some commonly employed approximations. While a simplified analysis of the steady-state depletion layer thickness in uniform shear suggests [13] $L_d \propto N_1 - N_2$, where N_1 and N_2 are the normal stress differences, it appears from Fig. 10 that the implicit assumption of the difference being independent of the position is not valid in Poiseuille flow for large Wi, Pe. It is, however, valid for steady shear flow near a single wall, where $Pe \rightarrow 0$ and $h \rightarrow \infty$.

The computations involving ensemble averages plotted in Fig. 9 and Fig. 10 have two limitations. First, as the distribution function tends to infinity close to the walls (due to the above approximations), we exclude the near-wall region $y < 0.5$, accounting for approx. 6% of the channel height. Second, as the perturbation series expansion of the distribution function converges only for small Wi, Pe [2], we restrict the ranges of Wi and Pe accordingly.
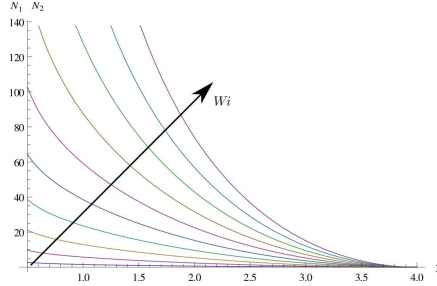
Fig. 10: The difference of normal stress differences N_1 and N_2 (scaled by nk_bT) across the channel width, with $b = 100, Pe = 1$ and $Wi = 0.5, 1, 1.5, \ldots 5$.

4 Stokeslet in Debye-Hückel electrolyte

In what follows, we denote the Green's function of the Stokes equation with a point charge and a counterion cloud as the electrophoretic Stokeslet.

4.1 Migration tensors for the electrophoretic Stokeslet

While the use of the HI tensor $\mathbf{\Omega}$ in Eq. 2 is sufficient for a pure dielectric medium, the presence of an electrolyte requires that all functions of $\mathbf{\Omega}$ that appear in the terms containing $\mathbf{F}^e$ be replaced by the corresponding functions of the electrophoretic HI tensor $\mathbf{\Omega}^e_{ij} \equiv (1 - \delta_{ij})\mathbf{S}^e_{ij} + \mathbf{G}^e_{ij}$, with the Long-Ajdari electrophoretic Stokeslet $\mathbf{S}^e$ and the associated wall correction $\mathbf{G}^e$. The aim of this section is to derive and evaluate these tensorial functions, namely the modified forms of the dyads $\bar{\mathbf{\Omega}}, \bar{\bar{\mathbf{\Omega}}}$ and $\mathbf{D_K}$, and write them in terms of the corresponding migration tensors. These tensors are needed to calculate the center-of-mass (n) and end-to-end (ψ) distribution functions in the vicinity of a single wall as well as in a slit, under the influence of a uniform electric field. The errors that arise when the electrophoretic wall correction $\mathbf{G}^e$ is neglected or replaced by the wall correction to the regular Stokeslet $\mathbf{G}$ are discussed in more detail in our previous work on Brownian dynamics [8].

For small inverse Debye lengths, $\kappa = \lambda_D^{-1}$, we can work with the entire electrophoretic Stokeslet, given by [12]

$$S^e_{ij} = \frac{e^{-\kappa r}}{4\pi\eta r} \left(\frac{2}{3}\delta_{ij} + \frac{1}{(\kappa r)^2} \left(1 + \kappa r + \frac{(\kappa r)^2}{3} - e^{\kappa r} \right) \left(\delta_{ij} - 3\frac{\hat{r}_i\hat{r}_j}{r^2} \right) \right), \quad (28)$$

where we adopt the standard tensor notation (see e.g. [14]), $r = |\hat{\boldsymbol{r}}|$ and $\hat{\boldsymbol{r}} = \boldsymbol{r} - \boldsymbol{r_0}$.

17

Using Taylor series expansions for $e^{\kappa r}$ and $e^{-\kappa r}$ and neglecting terms of third order and higher, we get

$$S^e_{ij} = f(\kappa r)\bar{S}_{ij},$$

where $f(\kappa r) = 1 - \kappa r + \frac{1}{2}(\kappa r)^2$ and $\bar{S}_{ij}$ is the usual Green's function of the Stokes flow, $\frac{1}{8\pi\eta r}\left(\delta_{ij} + \frac{\hat{r}_i\hat{r}_j}{r^2}\right)$, which one recovers in the limit of $\kappa \to 0$, i.e. when the electric field has been screened out entirely over the distance r. Upon calculating the other contributions to the image system near a planar wall [3], i.e. the potential dipole,

$$PD^e = \frac{1}{2}[(-1)^{j+1}\Delta S^e_{ij}]_{1\leq i,j\leq 3} = f(\kappa r)\bar{PD}_{ij} + h.o.t.,$$

and Stokeslet doublet

$$SD^e = [(-1)^{j+1}\frac{\partial S^e_{i2}}{\partial r_j}]_{1\leq i,j\leq 3} = f(\kappa r)\bar{SD}_{ij} + h.o.t.,$$

we note that the higher order terms in both PD^e and SD^e are of $\frac{1}{r^j}$, with $j \geq 3$. Thus, for $\kappa \approx 0$ and $r \gg 0$ (in accordance with the previous approximation in Taylor series), they may be neglected; the image system is then identical to the one worked out by Ma [13] and Kekre [9], with S, PD and SD defined as above.

In most situations of physical interest [12], only the algebraically decaying part of the electrophoretic Stokeslet (Eq. 28), $\boldsymbol{S^E}(\boldsymbol{r}) = \frac{1}{4\pi\eta\kappa^2}(\frac{\boldsymbol{I}}{r^3} - 3\frac{\boldsymbol{rr}}{r^5})$, needs to be retained. Note that this long-range contribution has, save for the constant, the same form as the potential dipole (Fig. 11), $\boldsymbol{D}(\boldsymbol{r}) = 4\pi\eta\kappa^2\boldsymbol{S^E}(\boldsymbol{r})$, since an ion surrounded by its counterion cloud has a net dipolar character. Thus, we can use the image system developed for a single wall [14, 4], extend it to a slit geometry and compute the required functions of $\boldsymbol{\Omega}$. The image system $\boldsymbol{D^W}$ consists of a superposition of the free-space dipole $\boldsymbol{D}$ and other degenerate singularities, namely Stokeslet quadruple $\boldsymbol{G^Q}$ and potential quadruple $\boldsymbol{Q}$, defined in Appendix A. In analogy to the splitting given in Eq. 3, we define the HI tensor as

$$\boldsymbol{\Omega}_{\alpha\beta} = \frac{1}{4\pi\eta\kappa^2}[\boldsymbol{D^W}(\mathbf{r}_\alpha, \mathbf{r}_\beta) - \delta_{\alpha\beta}\boldsymbol{D}(\mathbf{r}_\alpha - \mathbf{r}_\beta)], \tag{29}$$

where

$$\boldsymbol{D^W}(\mathbf{r}, \mathbf{r}_0) = \boldsymbol{D}(\hat{\mathbf{r}}) + \sum_{w=1}^{2} \boldsymbol{G}(\hat{\mathbf{R}}^w) \tag{30}$$
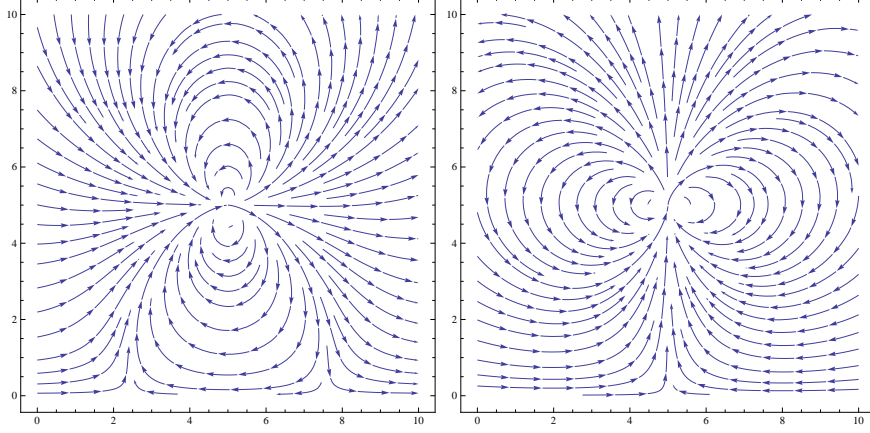
18

Fig. 11: Velocity field due to a potential dipole of unit strength located at $(x, y) = (5, 5)$ and oriented parallel (left) and perpendicular (right) to the wall at $y = 0$.

and the correction due to the two walls $G_{ij}(\hat{\mathbf{R}}^w) =$

$$(-1)^{j+1}[D_{ij}(\hat{\mathbf{R}}^w) + 2G^Q_{i22j}(\hat{\mathbf{R}}^w) - 2\left(y_0 - (w-1)H\right)Q_{i2j}(\hat{\mathbf{R}}^w) + 2D^*_{ij}(\hat{\mathbf{R}}^w)],\tag{31}$$

where the index w loops over the walls ($w = 1, 2$), α, β loop over the beads ($1 \leq \alpha, \beta \leq 2$) and i, j, k, l loop over the tensor components. Furthermore, we use

$$\hat{\mathbf{R}}^1 = \mathbf{r}_i - \mathbf{r}^{image}_j = \mathbf{r}_i - \mathbf{T}\,\mathbf{r}_j,\tag{32}$$

$$\hat{\mathbf{R}}^2 = \hat{\mathbf{R}}^1 - 2H\mathbf{e}_y,$$

where $\mathbf{T}$ is a Householder reflection in the bottom wall ($w = 1$), $\mathbf{T} = \mathbf{I} - 2\mathbf{e}_y\mathbf{e}_y$, see Fig. 12.

The required functions of $\boldsymbol{\Omega}$ are defined as

$$\bar{\boldsymbol{\Omega}} = \boldsymbol{\Omega}_{11} - \boldsymbol{\Omega}_{22} + \boldsymbol{\Omega}_{21} - \boldsymbol{\Omega}_{12},\tag{33}$$

$$\bar{\bar{\boldsymbol{\Omega}}} = \boldsymbol{\Omega}_{11} - \boldsymbol{\Omega}_{22} + \boldsymbol{\Omega}_{12} - \boldsymbol{\Omega}_{21},$$

$$\boldsymbol{D_K} = \frac{k_bT}{4}[\frac{2}{\zeta}\mathbf{I} + \boldsymbol{\Omega}_{11} + \boldsymbol{\Omega}_{22} + \boldsymbol{\Omega}_{12} + \boldsymbol{\Omega}_{21}].$$
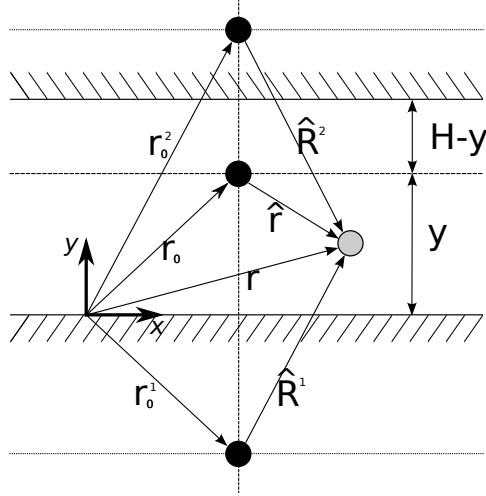
19

Fig. 12: The vector notation used for the image system in a slit. The image of vector $\mathbf{r}_i$, reflected in wall w is defined as $\mathbf{r}_i^w = \mathbf{T} \cdot \mathbf{r}_i + 2H(w-1)\mathbf{e}_y$.

4.1.1 Single wall

Assuming $|\mathbf{q}| \ll |\hat{\mathbf{R}}_c|$, we can linearize the tensors in Eq. 33 around $\hat{\mathbf{R}}_c$, $\hat{\mathbf{R}}_c = (\mathbf{I} - \mathbf{T}) \cdot \mathbf{r_c}$. After rewriting $\hat{\mathbf{R}}_{\alpha\beta}$ in terms of $\hat{\mathbf{R}}_c$ as

$$\hat{\mathbf{R}}_{\alpha\beta} = \hat{\mathbf{R}}_c + \frac{(-1)^i}{2}[\mathbf{q} + (1 - 2\delta_{ij})\mathbf{T} \cdot \mathbf{q}], \tag{34}$$

the linearization yields

$$\bar{\mathbf{\Omega}}^1 = \frac{1}{2\pi\eta\kappa^2} \left\{ [\mathbf{T} \cdot \mathbf{q}] \cdot [\nabla \boldsymbol{D} + 2\nabla \boldsymbol{G}^{\boldsymbol{Q}} + 2\nabla \boldsymbol{D}^*] - 2y\,(\mathbf{q} - 4\mathbf{e}_y) \cdot \nabla \boldsymbol{Q} + 2q_y \boldsymbol{Q}(\hat{\mathbf{R}}_c) \right\}, \tag{35}$$

$$\bar{\bar{\mathbf{\Omega}}}^1 = \frac{1}{2\pi\eta\kappa^2} \left\{ [-\mathbf{q}] \cdot [\nabla \boldsymbol{D} + 2\nabla \boldsymbol{G}^{\boldsymbol{Q}} + 2\nabla \boldsymbol{D}^* - 2y\nabla \boldsymbol{Q}] \right\}, \tag{36}$$

$$\boldsymbol{D_K}^1 = D_0 \left\{ \mathbf{I} + \zeta \boldsymbol{S}^{\boldsymbol{E}}(\mathbf{q}) \right\}. \tag{37}$$

These functions can now be expressed in terms of third order migration tensors,

$$\bar{\mathbf{\Omega}}^1 = \lambda^1 \bar{\boldsymbol{M}} \cdot \mathbf{q}, \tag{38}$$
$$\bar{\bar{\mathbf{\Omega}}}^1 = \lambda^1 \bar{\bar{\boldsymbol{M}}} \cdot \mathbf{q},$$

where $Q = |\mathbf{q}|$, $\mathbf{I}$ is a unit dyad and the superscript signifies the presence of a single wall. The elements of the constant migration tensors $\bar{\boldsymbol{M}}$ and $\bar{\bar{\boldsymbol{M}}}$ and the scalar function λ are tabulated in Appendix A.

20

4.1.2 Slit

In a slit with height H, the condition $|\mathbf{q}| \ll |\hat{\mathbf{R}}_c|$ can no longer be satisfied simultaneously for both walls. Linearizing instead around $\mathbf{q} = \mathbf{0}$ [9], we obtain

$$\bar{\boldsymbol{\Omega}}^{12} = (\lambda^1 + \lambda^2)\bar{\boldsymbol{M}} \cdot \mathbf{q}, \tag{39}$$
$$\bar{\bar{\boldsymbol{\Omega}}}^{12} = (\lambda^1 + \lambda^2)\bar{\bar{\boldsymbol{M}}} \cdot \mathbf{q},$$
$$\boldsymbol{D_K}^{12} = \boldsymbol{D_K}^1 - D_0\omega\left(\mathbf{I} + 3\mathbf{e}_y\mathbf{e}_y\right),$$

where the superscript signifies the presence of two parallel walls and the scalar function ω is defined in Appendix A.

4.2 Distribution function for the electrophoretic Stokeslet

To explore migration due to the separate and combined effects of flow and electrophoretic force within the limits of analytical theory, we neglect the terms proportional to W^{-n} where $n \geq 6$, on the same basis as discussed in Sec. 3.4. As our primary interest is in the near-wall behavior, we also do not include the diffusivity gradient, which we expect would slightly alter the concentration profiles near the centerline, in a manner similar to that observed in Fig. 2.

Analogously to Eq. 23, we obtain

$$\frac{\partial \ln \hat{n}(W)}{\partial W} = \frac{6M^E}{5h}WiPe + \frac{27M^Eh(h^2 - 2W)}{320W^4}Pe^2 + \frac{81N^Ea(h^2 - 4W)}{2hW^2}Wi^2, \tag{40}$$

where
$M^E(b) = \frac{\Gamma(b_{\frac{5}{2},1})}{\Gamma(b_{2,1})R^3\sqrt{\pi}}$, $N^E(b) = \frac{b_{7,5}}{b_{5,2}\,b_{7,2}^2}$ and we set the Debye length $\kappa^{-1} = R_g$.

Compared to the regular Stokeslet (Sec. 3.3,3.4 and 3.5), the distribution functions for the electrophoretic Stokeslet generally exhibit sharper transitions from the boundary layer to the core region, as apparent from Fig. 13-16, which show the concentration profiles for a chain with limited flexibility $(b = 1)$.

In a pure Poiseuille flow with no electric field, depicted in Fig. 13, we observe smaller depletion layer, especially for the Hookean model, and weaker dependence on the Weissenberg number for both FENE and Hookean dumbells. The distribution is approximately uniform throughout most of the
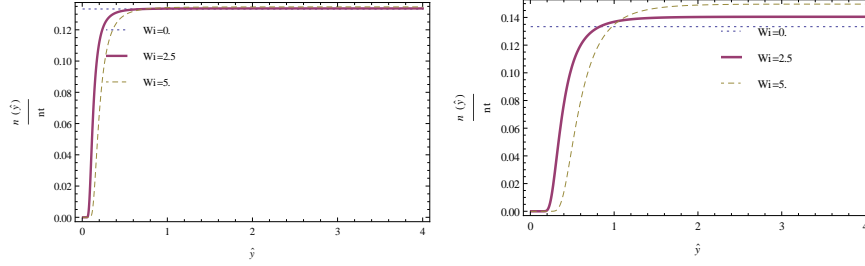
Fig. 13: Center-of-mass distribution for different Wi. No external force, diffusivity gradient neglected. Left: FENE spring model, right: Hookean spring model.
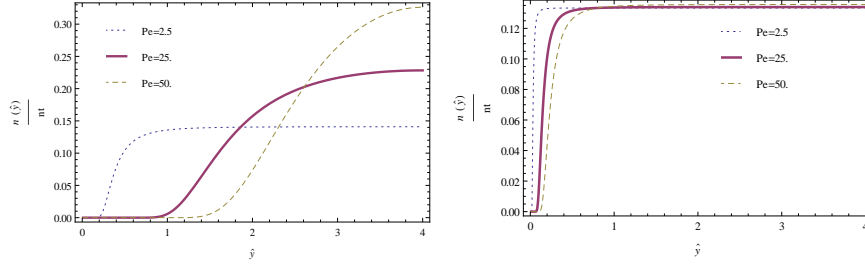

Fig. 14: Center-of-mass distribution for different Pe. No imposed flow. Left: FENE spring model, right: Hookean spring model.

cross-section. In pure electrophoresis with no imposed flow, depicted in Fig. 14, the difference in the depletion layer thickness (when compared to the regular Stokeslet) is even more pronounced for the Hookean model. The FENE model again shows thinner depletion layer for moderate Pe, but the layer does not grow as fast with Pe as it does for the regular Stokeslet, suggesting weaker scaling with the Peclet number. For combined pressure flow and electric field, Fig. 15 and 16 show qualitative differences between the FENE and Hookean models, which experience stronger and weaker migration away from the walls, respectively, compared to case of the regular Stokeslet. This is presumably due to smaller inter-bead separation distance for stiff FENE dumbells, which are affected by stronger HIs dominant at short distances due to the electrophoretic Stokeslet, which is associated with the electric force. A flexible Hookean dumbell, on the other hand, will exhibit larger extension; the beads will then interact primarily via regular HIs (associated with the spring and Brownian forces), dominant at longer distances. This difference becomes prominent only in strong migration patterns, such as when the flow and external force are combined. Migration
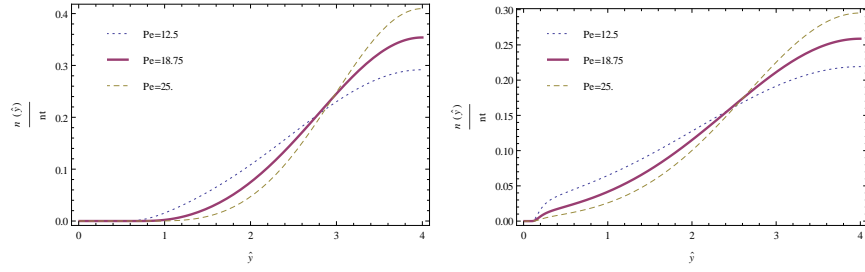
22

Fig. 15: Center-of-mass distribution. Flow and force in cooperation, $Wi = 5/6$. Left: FENE spring model, right: Hookean spring model.
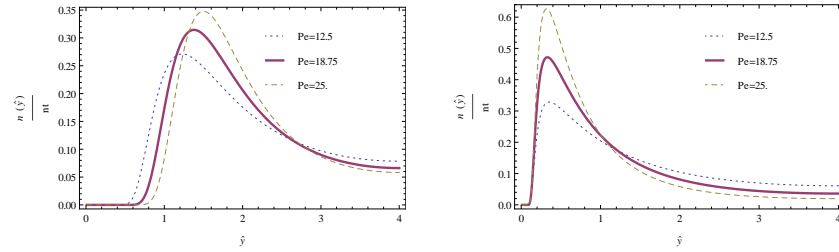

Fig. 16: Center-of-mass distribution. Flow and force in opposition, $Wi = 5/6$. Left: FENE spring model, right: Hookean spring model.

towards the wall, which arises when the electric field counteracts the pressure flow and is reflected in the $WiPe$ coupling term in Eq. 24, is enhanced for both Hookean and FENE models, as evidenced in Fig. 16 by the shift of the maxima in the concentration profile towards the walls.

We can conclude that qualitative differences in migration patterns and depletion layer thickness can be attributed to qualitatively different decay of the wall-mediated HIs due to the electrophoretic Stokeslet, with strong dependence on the flexibility of the polymer and the salt concentration of the solvent. We note that the above analysis of migration near solid interfaces in confinement is applicable to low Reynolds number flows associated with large Schmidt number $Sc = \frac{\nu}{D} \gg 1$, where ν is kinematic viscosity. For large Reynolds numbers, the chain will be convected away from the region of influence of the wall-mediated HIs (both regular and electrically-induced) by the time the velocity perturbation, reflected from the wall, can be detected. This effect will be further enhanced by the finite time of momentum transport in case of low Schmidt numbers, resulting in a negligible impact of HI-induced migration on chain dynamics under such conditions.

A   Electrophoretic migration tensors

In the vicinity of a planar wall, the singularities of the electrophoretic flow are the same as those of the potential dipolar flow. These include degenerate Stokeslet quadruples D_{ij}, D_{ij}^* and G_{ijkl}^Q, which are defined as follows:

$$D_{ij} = \frac{\delta_{ij}}{r^3} - 3\frac{x_i x_j}{r^5}, \tag{41}$$

$$G_{ijkl}^Q = \frac{1}{r^3}(\delta_{il}\delta_{jm} + \delta_{im}\delta_{il} - \delta_{ij}\delta_{lm})$$
$$- \frac{1}{r^5}(\delta_{lm}x_i x_j + \delta_{jm}x_i x_l + \delta_{jl}x_i x_m + \delta_{im}x_j x_l + \delta_{il}x_j x_m + \delta_{ij}x_l x_m)$$
$$+ \frac{15}{r^7}(x_i x_j x_l x_m), \tag{42}$$

$$Q_{ijl} = -\frac{3}{r^5}(\delta_{ij}x_l + \delta_{il}x_j + \delta_{jl}x_i) + 15\frac{x_i x_j x_l}{r^7}, \tag{43}$$

$$D_{ij}^* = \delta_{j2}D_{i2}. \tag{44}$$

In case of a single wall, we expand the hydrodynamic interaction tensors $\mathbf{\Omega}$ in Taylor series around $\hat{\mathbf{R}}_c$ and truncate at linear terms (assuming $Q < |\hat{\mathbf{R}}_c|$, only far-wall effects are considered), i.e. $\mathbf{\Omega}(\hat{\mathbf{R}}_c + \boldsymbol{\xi}) \approx \sum_{n=0}^{1} \frac{1}{n!}(\boldsymbol{\xi} \cdot \nabla)^n \mathbf{\Omega}(\hat{\mathbf{R}}_c)$, where $\boldsymbol{\xi}_{\alpha\beta} = \hat{\mathbf{R}}_c + \frac{(-1)^\alpha}{2}[\mathbf{q} + (1 - 2\delta_{\alpha\beta})\mathbf{T} \cdot \mathbf{q}]$ (cmp Eq. 32). In case of a slit

(two parallel planar walls), the expansion is around $\mathbf{q} = \mathbf{0}$. The linearized tensors can be expressed in terms of constant migration tensors $\bar{\boldsymbol{M}}$ and $\bar{\bar{\boldsymbol{M}}}$ (Eq. 38 and 39), whose non-zero components are listed in Table 1. The scalar functions $\lambda^w(y)$ and $\omega(y)$ are defined as

$$\lambda^w(y) = (-1)^{w-1} \frac{3}{32\pi\eta\kappa^2 \left[y - (w-1)H\right]^4}, \quad \text{for } w = 1, 2; \qquad (45)$$

$$\omega(y) = \frac{3a}{4\kappa^2} \left(\frac{1}{y^3} - \frac{1}{(y-H)^3}\right). \qquad (46)$$

Table 1: Migration tensors. From left to right: Non-zero values of $\bar{M}_{ijk}$ and $\bar{\bar{M}}_{ijk}$.

Value	ijk indices
5	211, 233
-3	112, 332, 121, 323
-10	222

Value	ijk indices
3	121, 323
-1	112, 332
-5	211, 233
-6	222

References

[1] A.V. Bhave, R.C. Armstrong, and R.A. Brown, *Kinetic theory and rheology of dilute, nonhomogeneous polymer solutions*, The Journal of chemical physics **95** (1991), no. 4, 2988–3000.

[2] R.B. Bird, R.C. Armstrong, and O. Hassager, *Dynamics of polymeric liquids. Vol. 1: Fluid mechanics*, (1987).

[3] JR Blake, *A note on the image system for a Stokeslet in a no-slip boundary*, Proc. Camb. Phil. Soc, vol. 70, Cambridge Univ Press, 1971, pp. 303–310.

[4] JR Blake and AT Chwang, *Fundamental singularities of viscous flow*, Journal of Engineering Mathematics **8** (1974), no. 1, 23–29.

[5] J.E. Butler, O.B. Usta, R. Kekre, and A.J.C. Ladd, *Kinetic theory of a confined polymer driven by an external force and pressure-driven flow*, Physics of Fluids **19** (2007), 113101.

[6] L. Fang, H. Hu, and R.G. Larson, *DNA configurations and concentration in shearing flow near a glass surface in a microchannel*, Journal of rheology **49** (2005), 127.

[7] M. Herrchen and H.C. Öttinger, *A detailed comparison of various FENE dumbbell models*, Journal of non-newtonian fluid mechanics **68** (1997), no. 1, 17–42.

[8] P. Hotmar and R. Chella, *Brownian dynamics of polymer migration in combined pressure-driven and electrophoretic flows*, pre-print.

[9] R. Kekre, *Role of hydrodynamic interactions in dynamics of semi-flexible polyelectrolytes*, (2011).

[10] R. Kekre, J.E. Butler, and A.J.C. Ladd, *Role of hydrodynamic interactions in the migration of polyelectrolytes driven by a pressure gradient and an electric field*, Physical Review E **82** (2010), no. 5, 050803.

[11] R.G. Larson, *The rheology of dilute solutions of flexible polymers: Progress and problems*, Journal of rheology **49** (2005), 1.

[12] D. Long and A. Ajdari, *A note on the screening of hydrodynamic interactions, in electrophoresis, and in porous media*, The European Physical Journal E: Soft Matter and Biological Physics **4** (2001), no. 1, 29–32.

[13] H. Ma and M.D. Graham, *Theory of shear-induced migration in dilute polymer solutions near solid boundaries*, Physics of Fluids **17** (2005), 083103.

[14] C. Pozrikidis, *Boundary integral and singularity methods for linearized viscous flow*, no. 8, Cambridge University Press, 1992.

[15] H. Risken, *The Fokker-Planck equation: Methods of solution and applications*, vol. 18, Springer Verlag, 1996.

[16] O.B. Usta, J.E. Butler, and A.J.C. Ladd, *Transverse migration of a confined polymer driven by an external force*, Physical review letters **98** (2007), no. 9, 98301.

[17] N.J. Woo, E.S.G. Shaqfeh, and B. Khomami, *Effect of confinement on dynamics and rheology of dilute DNA solutions. I. Entropic spring force under confinement and a numerical algorithm*, Journal of Rheology **48** (2004), 281.